ADVANCED ENERGY MATERIALS
www.advenergymat.de

Collectively Exhaustive Hybrid Triboelectric Nanogenerator Based on Flow-Induced Impacting-Sliding Cylinder for Ocean Energy Harvesting

Ji-Seok Kim, Junyoung Kim, Jong-Nam Kim, Junseong Ahn, Jun-Ho Jeong, Inkyu Park, Daegyoum Kim, and Il-Kwon Oh**

For the sustainable application of remote sensing and monitoring in the ocean environment, energy harvesting technology based on flow-induced vibration is in the spotlight. Herein, based on the flow-induced self-excitation of an impacting-sliding cylinder, a collectively exhaustive hybrid triboelectric nanogenerator (TENG) is reported, that utilizes both free-standing-sliding (FS) and contact-separation (CS) modes. Most importantly, the flow-induced impacting cylinder (FIC) between two side walls is newly implemented to resolve the critical problem of the lock-in phenomena occurring in conventional vortex-induced vibration systems of circular cylinders. Owing to the presence of two side walls, the FIC based TENG (FIC-TENG) shows a stable electrical power generation in a wide range of flow velocity (0.05–1.02 m s^{-1}) without lock-in phenomena. In addition, the collectively exhaustive FIC-TENG can be used to continuously produce electric power utilizing both FS and CS hybrid modes. The energy harvesting performance is greatly enhanced by adopting nanopatterns on triboelectric surfaces in the CS mode TENG and a frequency upconversion effect of interdigitated electrodes in the FS mode TENG, resulting in proper remote operation of a wireless fidelity thermometer.

1. Introduction

The environmental destruction caused by fossil fuels for electricity generation and the depletion of energy have led to a continuous interest in renewable energy.[1] With the development of the Internet of Things which requires billions of sensors, scavenging natural energy from sources such as wind, tide, and solar has been reported using such technologies as electromagnetic induction,[2] triboelectricity,[3] piezoelectricity,[4] solar cells,[5] and hybrid devices[6] to replace batteries. Specifically, hydrokinetic energy is promising as a next-generation eco-friendly energy source because it can produce tremendous energy in the ocean which covers 70% of the earth.[7] However, conventional hydrokinetic energy harvesters using electromagnetic generators have been considered to be large in scale, expensive, and low in efficiency due to their low operating frequency.[8]

Recently, triboelectric nanogenerators (TENGs) have been intensively studied as a novel way to replace existing hydrokinetic energy harvesters by taking advantage of effective power generation that is possible even with mechanical movements in low-frequency ocean waves (0.2–0.7 Hz).[9] TENGs harvest electrical energy using a coupling effect of triboelectrification and electrostatic induction;[10] the basic operating modes of TENGs are classified as contact-separation (CS),[11] lateral sliding,[12] freestanding sliding (FS),[13] and single electrode[14] modes. To harvest hydrokinetic energy, TENGs based on the solid–liquid contact electrification have been considered due to its large effective contact area at the solid–liquid interface, however the solid–liquid TENGs should address various limitations which reduce the output power (e.g. low solid–liquid contact force, hydrophilicity of solid surfaces, and salinity of ocean water).[15] Since TENGs are simple to manufacture, inexpensive, and available at small scale, many studies have been conducted to generate power by arranging floating buoy-type TENGs in the ocean as networks.[16] Floating buoy-type TENGs harvest electrical energy by oscillating like ocean waves at sea level; however, there are concerns that output power is poorly limited in calm waves and that such devices

J.-S. Kim, J.-N. Kim, I.-K. Oh
National Creative Research Initiative for Functionally Antagonistic Nano-Engineering
Department of Mechanical Engineering
School of Mechanical and Aerospace Engineering
Korea Advanced Institute of Science and Technology (KAIST)
291 Daehak-ro, Yuseong-gu, Daejeon 34141, Republic of Korea
E-mail: ikoh@kaist.ac.kr

J. Kim, J. Ahn, I. Park, D. Kim
Department of Mechanical Engineering
School of Mechanical and Aerospace, Engineering
Korea Advanced Institute of Science and Technology (KAIST)
291 Daehak-ro, Yuseong-gu, Daejeon 34141, Republic of Korea
E-mail: daegyoum@kaist.ac.kr

J.-H. Jeong
Research Planning and Coordination Division
Korea Institute of Machinery and Materials (KIMM)
156 Gajeongbuk-ro, Yuseong-gu, Daejeon 34103, Republic of Korea

The ORCID identification number(s) for the author(s) of this article can be found under https://doi.org/10.1002/aenm.202103076.

DOI: 10.1002/aenm.202103076

 © 2021 Wiley-VCH GmbH

Check for updates
16146840, 2022, 3, Downloaded from https://onlinelibrary.wiley.com/doi/10.1002/aenm.202103076 by Korea Advanced Institute Of, Wiley Online Library on [21/11/2022]. See the Terms and Conditions (https://onlinelibrary.wiley.com/terms-and-conditions) on Wiley Online Library for rules of use; OA articles are governed by the applicable Creative Commons License

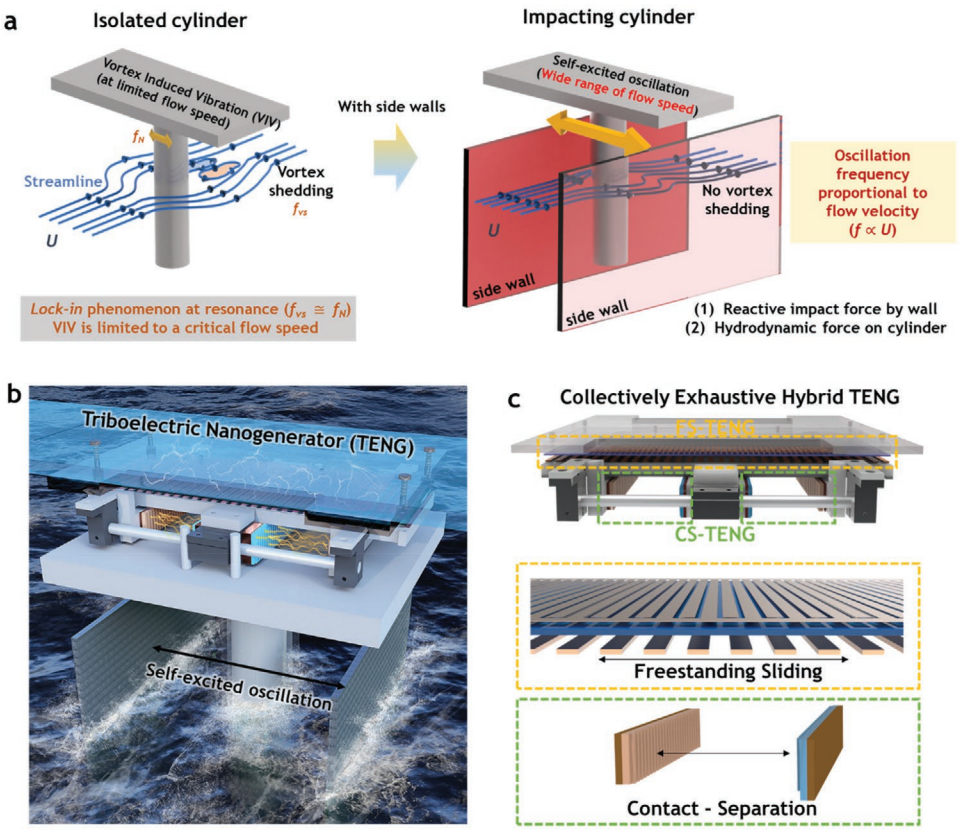


Figure 1. Flow structure and collectively exhaustive hybrid FIC-TENG based on FIC for ocean energy harvesting. a) Schematic illustration of flow structures of isolated cylinder and impacting cylinder. b) Schematic illustration of collectively exhaustive hybrid TENG in ocean. c) Schematic diagram of detailed operating modes of hybrid FIC-TENG structure.

may become marine debris due to the risk of breakage in rough waves.[17]

To address the aforementioned limitations, a cylindrical structure undergoing vortex-induced vibration (VIV) was suggested as a novel system to extract electrical energy from fluid flow.[18] When a circular cylinder is immersed in fluid flow, a pair of counter vortices is continuously shed from the surface of the cylinder. A periodic lift force is exerted on the cylinder due to the shed vortices, and the cylinder is forced to oscillate.[19] In most studies of VIV-based energy harvesters, the cylinder is connected to a flexible beam and a piezoelectric patch is attached to the beam. The piezoelectric patch, deformed by the VIV motion of the cylinder, is used to convert hydrokinetic energy to electrical energy.[20] However, there is a critical disadvantage in applying the VIV motion of the cylinder to the energy harvesting devices. Since the VIV is a resonance-based vibration phenomenon, the circular cylinder can show large-amplitude oscillation only in a limited range of flow velocity, so called the lock-in region at which the resonance between the vortex shedding frequency and the natural frequency of the oscillating cylinder system occurs as shown in **Figure 1**a.

Here, a novel flow-induced impacting-sliding cylinder TENG (FIC-TENG) using both FS and CS modes in combination with the self-excited oscillation of a cylinder between two side walls is proposed. To the best of our knowledge, a collectively exhaustive triboelectric energy harvester utilizing FIC in water is for the first time developed to convert hydrokinetic energy in the ocean into electricity. In addition, the proposed FIC-TENG realizes a novel design in which the cylindrical bluff body continuously oscillates by placing two side walls in the water to resolve the critical problem of the lock-in phenomena in the conventional VIV energy harvesting system. The two side walls are placed close together so that they can impact the cylinder when the cylinder undergoes flow-induced vibration (FIV). In addition, the output performance of the suggested FIC-TENG can be greatly improved because the operating frequency of the FIC-TENG increases linearly as the flow velocity increases. Figure 1 provides a schematic illustration of the collectively exhaustive hybrid FIC-TENG that converts the motion of the FIC into electrical energy in the ocean environment. The flow structures of an isolated cylinder and the impacting cylinder are schematically illustrated in Figure 1a. For the isolated cylinder, the hydrodynamic force induced by the vortex shedding behind the cylinder enforces the cylinder to oscillate. With the impact on the side walls, the reactive force from the walls is exerted on the cylinder as an external impact force. Besides, the impact changes the flow structure around the cylinder and the hydrodynamic force is applied to the surface of the cylinder. As a result, the impacting cylinder maintains large-amplitude oscillation from low to high free-stream velocity and shows significantly high oscillation frequency while oscillating in a range

© 2021 Wiley-VCH GmbH

16146840, 2022, 3, Downloaded from https://onlinelibrary.wiley.com/doi/10.1002/aenm.202103076 by Korea Advanced Institute Of, Wiley Online Library on [21/11/2022]. See the Terms and Conditions (https://onlinelibrary.wiley.com/terms-and-conditions) on Wiley Online Library for rules of use; OA articles are governed by the applicable Creative Commons License

of free-stream velocity much higher than the region of free-stream velocity where the isolated cylinder cannot oscillate.

Furthermore, the FIC-TENG utilizes the FS mode TENG (FS-TENG) which can generate electrical energy of relatively higher frequency by using interdigitated electrodes compared with the frequency of input mechanical oscillation, and a high current density due to the frequency upconversion effect.[21] Moreover, using a nanopatterned Si stamp, the CS mode TENG (CS-TENG) greatly improves TENG output power by introducing a nanopattern on the surface of UV curable polymers.[22] The structure of the collectively exhaustive FIC-TENG in the ocean is schematically illustrated in Figure 1b. Since the conventional FS-TENGs harvest electrical energy through the relative lateral sliding motion of two frictional surfaces, the slider stops when the sliding direction is changed with zero speed, and at the moment there is no kinetic energy to be harvested.[23] In addition, the conventional CS-TENG also generates impulse-type electrical signals only at the moment of contact and separation, so most kinetic energy during the reciprocating motion is not converted to electricity, resulting in high instantaneous power, but very low time-averaged power.[24] Most importantly, the collectively exhaustive FIC-TENG can overcome the drawbacks of both FS-TENG and CS-TENG with synergy of continuous energy harvesting. The FS-TENG uses collision with the side wall when the slider changes the sliding direction to minimize the loss of kinetic energy by changing the direction due to the coefficient of restitution, and the impact energy during the collision can be effectively converted into electrical energy through CS-TENGs. The collectively exhaustive hybrid FIC-TENG utilizes the FS-TENG and the CS-TENG on the surface, where all relative motions (sliding and CS) occur except for the power transmission part to transmit cylinder oscillation to the energy harvesting module (Figure 1c). Therefore, the FIC-TENG has a great advantage in that it can continuously convert the mechanical energy of the FIC into electrical energy.

In this study, a water tunnel experiment is conducted and structural components such as air bushings, springs, side walls, and shafts are specially designed to make the cylinder to have only 1D linear oscillation (Figure S1, Supporting Information). The energy harvesting performances of FS-TENG and CS-TENG in the FIC-TENG, depending on the free-stream velocity, gap distance between two side walls, and other parameters, are systematically optimized. Furthermore, the collectively exhaustive energy harvesting performance of the FIC-TENG in a broad range of flow velocities is validated with fluid flow experiments. The collectively exhaustive hybrid FIC-TENG capable of continuously generating electricity with seamless synergy between FS and CS modes can provide an efficient way to effectively harvest water wave energy for self-powered sensor networks in ocean.

2. Results and Discussion

2.1. Flow-Induced Oscillation and Periodic Impact of Cylinder

To evaluate the energy harvesting performance of the TENG system equipped with the circular cylinder, water tunnel experiments were conducted (Video S1, Supporting Information). A schematic diagram and optical image of the suggested FIV system are provided in Figure S2, Supporting Information. A closed-loop water tunnel with an open test section having 0.5 m width and 1.2 m length was used; the height of the free surface from the bottom of the test section was fixed as 0.4 m. The experiments were conducted with a free-stream velocity of up to 1.00 m s^{-1}. An aluminum cylinder with a diameter of $D = 5$ cm was attached to the TENG system. The acrylic walls were arranged parallel to the free stream on both sides of the cylinder. The streamwise length of the walls was fixed as $w/D = 8.0$. The dimensionless gap ratio, the distance between the cylinder surface and the side wall divided by the diameter of the cylinder, varied from $e/D = 0.2$ to $e/D = 0.4$.

First, we compare the dynamics of the isolated cylinder without side walls and the impacting cylinder with gap ratio of $e/D = 0.3$ to identify the dynamical change induced by periodic impact between the cylinder and the side walls, which is expected to greatly affect the energy harvesting performance. The dimensionless amplitude, A/D, and the frequency ratio, f/f_n, are plotted in **Figure 2**a,b as a function of the free-stream velocity; f is the oscillation frequency of the cylinder, and f_n is the natural frequency of the cylinder in water, $f_n = 0.53$ Hz. In Figure 2a, the isolated cylinder shows the general lock-in phenomenon of VIV; the circular cylinder oscillates only in the limited range of the free-stream velocity at which the cylinder can resonate with the oscillating frequency in accordance with the frequency of vortex shedding. In general, the isolated cylinder is subjected to the sinusoidal lift force as expressed as:

$$F_L = F_L^0 \sin\left(2\pi f_{vs} t\right) \tag{1}$$

where F_L^0 is the amplitude of the lift force and f_{vs} is the vortex shedding frequency. When the f_{vs} matches f_n, the cylinder undergoes lock-in. The cylinder starts to oscillate from $U = 0.11$ m s^{-1}. The oscillation amplitude increases and reaches the peak amplitude, $A/D = 0.95$ at $U = 0.16$ m s^{-1} due to resonant effect between the frequency of the sinusoidal lift force and the natural frequency of the isolated cylinder. Thereafter, the amplitude decreases, and the cylinder maintains small amplitude oscillation beyond $U = 0.27$ m s^{-1}. In Figure 2b, the two blue dashed lines represent the vortex shedding frequency of the fixed cylinder ($St = f \cdot D/U = 0.2$) and the natural frequency of the oscillating system ($f/f_n = 1$). In general, resonance of the isolated cylinder occurs near a critical free-stream velocity, where the two lines intersect on the graph. At $U = 0.11$ m s^{-1}, when the cylinder starts to oscillate, the St of the isolated cylinder is almost 0.2 and the oscillation frequency is the natural frequency of the oscillating system. With the increase of the free-stream velocity, the dimensionless frequency converges to $f/f_n = 1.2$.

On the other hand, with side walls of $e/D = 0.3$, the oscillating cylinder periodically impacts the side walls and thus exhibits dramatically different responses from those of the isolated cylinder (Figure 2a,b). Above the critical velocity at which the cylinder starts to impact the side walls, the impacting cylinder maintains oscillation up to the high free-stream velocity outside of the lock-in region of the isolated cylinder. And, because of the gap flow between the cylinder and the side walls, the impacting cylinder starts to oscillate from $U = 0.05$ m s^{-1}, which is much lower than the critical flow speed of the isolated

© 2021 Wiley-VCH GmbH

16146840, 2022, 3, Downloaded from https://onlinelibrary.wiley.com/doi/10.1002/aenm.202103076 by Korea Advanced Institute Of, Wiley Online Library on [21/11/2022]. See the Terms and Conditions (https://onlinelibrary.wiley.com/terms-and-conditions) on Wiley Online Library for rules of use; OA articles are governed by the applicable Creative Commons License

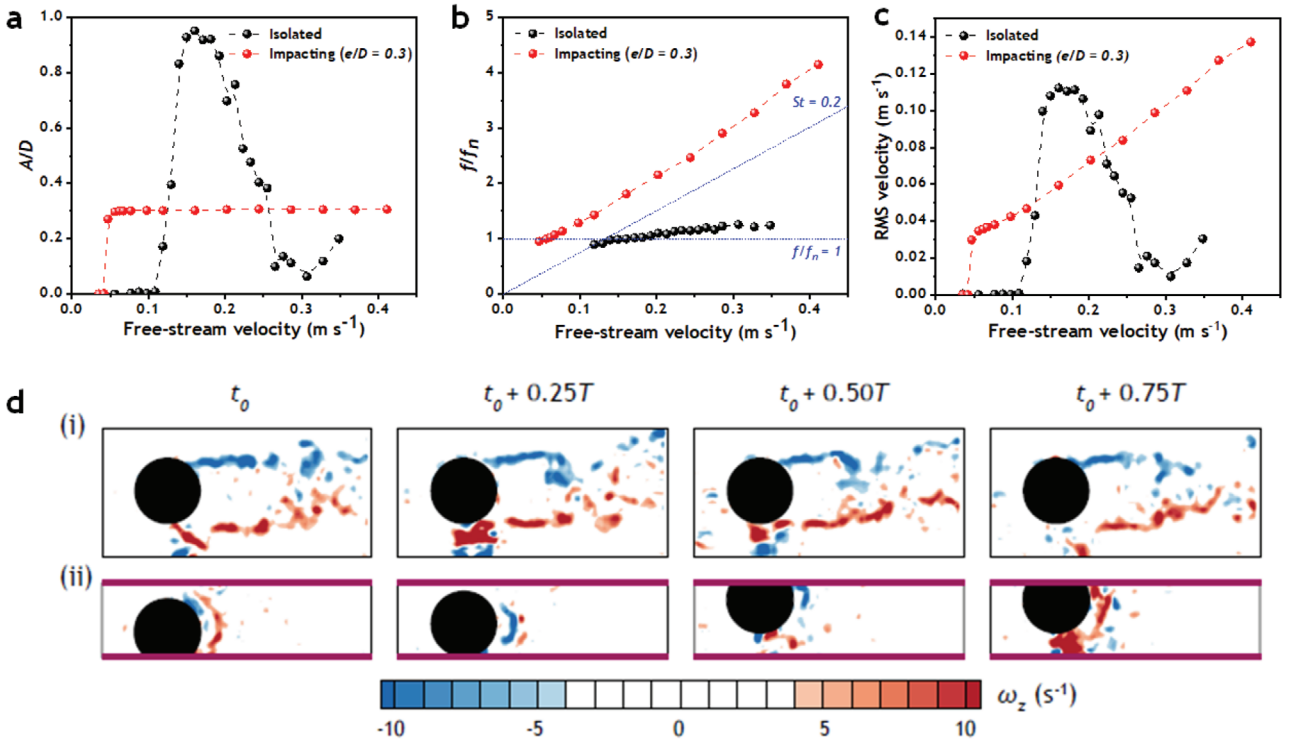


Figure 2. FIV results of proposed FIC model. Comparison of dynamics according to free-stream velocity between isolated cylinder and impacting cylinder. a) Dimensionless amplitude (A/D), b) dimensionless frequency (f/f_n), and c) RMS velocity of cylinder. d) Vorticity field near cylinder during one cycle of oscillation; Without side walls (isolated) (i), and with side walls ($e/D = 0.3$) (ii).

cylinder, $U = 0.11$ m s^{-1}. Since the movement of the impacting cylinder is confined by the side walls, the dimensionless amplitude is the same as the e/D value. Besides this, the oscillation frequency increases continuously in proportion to the free-stream velocity. As a result, although the oscillation amplitude of the impacting cylinder is limited by the gap ratio, the high oscillation frequency induces a faster transverse velocity of the cylinder than that of the isolated cylinder. In Figure 2c, the root mean square (RMS) transverse velocity of the two cylinders with and without the side walls are compared. The RMS velocity is calculated as follows:

$$v_{\mathrm{RMS}} = \sqrt{\frac{1}{T}\int_0^T v^2(t)\,dt} \tag{2}$$

where v is the instantaneous transverse velocity of the cylinder and T is the measurement time of several cycles. Although, within the lock-in region, the RMS velocity of the isolated cylinder is greater than that of the impacting cylinder, the impacting cylinder shows a significantly larger transverse velocity than the isolated cylinder from $U = 0.24$ m s^{-1}. To compare the flow structure near the cylinder without and with the impact, we conducted particle image velocimetry (PIV). In the PIV experiment, the small particles immersed in the water is illuminated by laser sheet and photographed in short interval. By correlating the images, we can visualize the flow field. In Figure 2d, the periodic vortex shedding is well developed behind the isolated cylinder. However, with the impact, the shear layer developed near the cylinder does not shed from the cylinder, and the periodic vortex shedding does not occur. Therefore, the limitation of the isolated circular cylinder oscillating only in a very narrow flow velocity range due to resonance is overcome by placing side walls, using the FIV phenomenon rather than the resonance-based VIV phenomenon, in which the vortex shedding frequency and the natural frequency of the circular cylinder match.

2.2. Energy Harvesting Performance of Collectively Exhaustive FIC-TENG

To investigate the energy harvesting performance of the hybrid mode FIC-TENG, water tunnel experiments were conducted. A schematic diagram of the fabricated FIC-TENG structure is provided in **Figure 3**a, and two operating modes of the FIC-TENG, the FS-TENG and the CS-TENG, are shown separately in Figure 3b. Figure S3, Supporting Information, provides the optical images of the stator and slider of the FS-TENG. To effectively transmit the oscillation of the cylinder to the moving parts of the FIC-TENG, bearings were placed between the rods on the plate above the cylinder to reduce friction of the shafts. Then, the slider of the FS-TENG was attached to the top of the bearing, a moving part of the CS-TENG was placed on the left and right sides of the bearing, and the stationary part of the CS-TENG was fixed to the side of the shaft support to induce relative motion of CS and sliding through bearing oscillation.

© 2021 Wiley-VCH GmbH

16146840, 2022, 3, Downloaded from https://onlinelibrary.wiley.com/doi/10.1002/aenm.202103076 by Korea Advanced Institute Of, Wiley Online Library on [21/11/2022]. See the Terms and Conditions (https://onlinelibrary.wiley.com/terms-and-conditions) on Wiley Online Library for rules of use; OA articles are governed by the applicable Creative Commons License

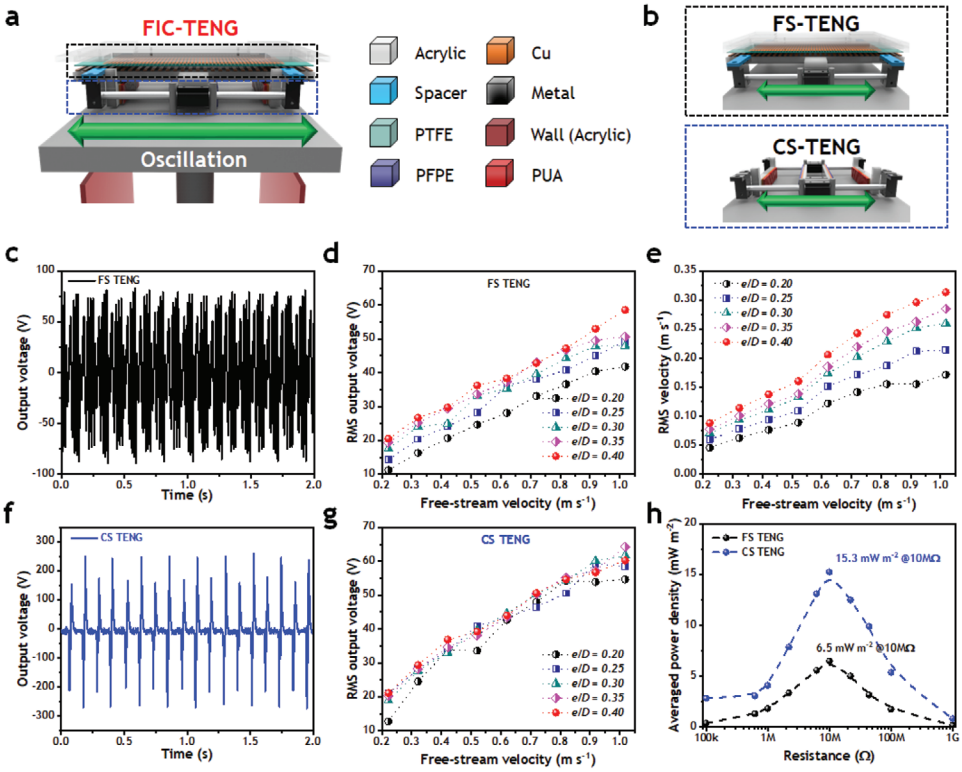


Figure 3. Electrical characterization of FIC-TENG. a) Schematic illustration of FIC-TENG. b) Schematic diagram of FS-TENG and CS-TENG in FIC-TENG. c) V of FS-TENG in FIC-TENG at free-stream velocity of 1.02 m s^{-1}. d) V_{RMS} of FS-TENG in the FIC-TENG at different free-stream velocities and gap ratios (e/D). e) RMS velocity of cylinder. f) V of CS-TENG in FIC-TENG at free-stream velocity of 1.02 m s^{-1}. g) V_{RMS} of CS-TENG in FIC-TENG at different free-stream velocities and gap ratios (e/D). h) Averaged power densities of FS-TENG and CS-TENG under different load resistances.

As the sliding friction of the FS-TENG increases, the triboelectric energy harvesting performance is enhanced. However, if the frictional force becomes too large, the cylinder does not oscillate. Thus, spacers that adjust the distance between the slider and the stator of the FS-TENG are placed between the shaft supports and the base plate to control the frictional force. To optimize the energy harvesting performance of the FS-TENG in the FIC-TENG, the RMS value of the output voltage (V_{RMS}) of the FS-TENG was calculated as follows:

$$V_{RMS} = \sqrt{\frac{1}{T}\int_0^T V^2(t)\,dt} \tag{3}$$

where V_{RMS} is the RMS value of the output voltage (V) and T is the time period, measured with an oscilloscope (Figure S4, Supporting Information). In the case of the thickness of 3.7 mm, the frictional force is too high, the cylinder only oscillates in high free-stream velocities, and the V_{RMS} values are relatively low because oscillating frequency of the FIC is also affected by the frictional force. In the case of thickness of 4.5 mm, the FIC oscillates at all free-stream velocities; however, the V_{RMS} is very low in all free-stream velocities because of low frictional force. Therefore, the thickness of the spacer was optimized to 4.3 mm because this thickness induces the highest V in all free-stream velocities and the vibration of the cylinder is confirmed in a relatively wide free-stream velocity range. An optical image of experimental specimen of the FS-TENG and CS-TENG in the FIC-TENG is shown in Figure S5, Supporting Information. Figure S6, Supporting Information, provides an optical image of the water tunnel experimental setup. The acrylic wall and aluminum cylinder are placed inside the water tunnel, and the energy harvesting module is fixed at the top. Microparticles were immersed in the circulating water tunnel and high-speed camera was placed below transparent acrylic plate of the water tunnel for the PIV.

The time series of the V signal of the FS-TENG in the FIC-TENG was measured at the free-stream velocity of 1.02 m s^{-1} (Figure 3c). Because the interval between the interdigitated electrodes of the FS-TENG is smaller than the gap distance between the cylinder and the side walls, the FS-TENG generates multiple peaks of V per cycle of cylinder oscillation. With high oscillation frequency, the FS-TENG shows an extremely small dead zone that has no electrical output signal. To optimize the performance of the FS-TENG in the FIC-TENG, the V_{RMS} value of the FS-TENG was evaluated while changing the gap ratio and free-stream velocity, as shown in Figure 3d. For the entire range of free-stream velocity, the FS-TENG shows a higher V_{RMS} for a larger gap ratio. To demonstrate the velocity effect on the V_{RMS} of the FS-TENG, the RMS velocities of the impacting cylinder were calculated with different gap ratios. Improvement of the V_{RMS} of the FS-TENG can be attributed to the increase of the RMS velocity of the cylinder (Figure 3e). In particular, as the gap ratio becomes greater, the amplitude of

© 2021 Wiley-VCH GmbH

16146840, 2022, 3, Downloaded from https://onlinelibrary.wiley.com/doi/10.1002/aenm.202103076 by Korea Advanced Institute Of, Wiley Online Library on [21/11/2022]. See the Terms and Conditions (https://onlinelibrary.wiley.com/terms-and-conditions) on Wiley Online Library for rules of use; OA articles are governed by the applicable Creative Commons License

the cylinder oscillation increases while the oscillation frequency tends to decrease slightly at the same free-stream velocity. The amplitude of cylinder oscillation has a more dominant effect on the RMS velocity and the V_{RMS} of the FS-TENG than does the oscillation frequency because the V_{RMS} of the FS-TENG tends to increase as the distance between the side walls increases. In addition, it should be noted that, compared with the conventional FIV system, the FIC-TENG is considerably more efficient for ocean energy harvesting because it can convert mechanical vibrational energy into electric energy while maintaining large-amplitude oscillation in a significantly wide range of flow velocity.

Figure 3f shows the V of the CS-TENG in the FIC-TENG when the free-stream velocity is 1.02 m s^{-1}. The CS-TENG shows very different results from the FS-TENG. Since the nano-patterned surfaces of the CS-TENG come into contact twice per cycle, the frequency of the V is lower than that of the FS-TENG. Notably, the peak V of the CS-TENG is about four times that of the FS-TENG. For comparison, the V_{RMS} of the CS-TENG was also calculated with different gap ratios and free-stream velocities (Figure 3g). In the CS-TENG, the V_{RMS} also tends to obviously increase with the free-stream velocity because the contact force increases. However, the effect of the gap ratio on the V_{RMS} of the CS-TENG is relatively insignificant. As the gap ratio increases, the separation distance between the contact surfaces gradually increases in the CS-TENG. Even if the distance between the two contact surfaces increases by more than a certain level, the potential difference is saturated, yielding little influence on the V_{RMS} of the CS-TENG in the FIC-TENG. To investigate the effect of the gap ratio more clearly, the V_{RMS} values of the FS-TENG and CS-TENG in the entire free-stream velocity range were averaged for each gap ratio (Figure S7, Supporting Information). For performance optimization of the FIC-TENG, the gap ratio was determined to be 0.4, and further experiments were conducted with a gap ratio of 0.4 and a flow velocity of 1.02 m s^{-1}. Also, the rectified output voltage of the FS-TENG and CS-TENG at a free-stream velocity of 1.02 m s^{-1} was measured to validate the feasibility of the proposed FIC-TENG for power management applications in Figure S8, Supporting Information. The output voltages of both CS-TENG and FS-TENG were measured with an external electrical load from 100 kΩ to 1 GΩ, and the averaged power (P_{ave}) values of the FS-TENG and CS-TENG were calculated as follows:

$$P_{ave} = \frac{V_{RMS}^2}{R_{load}} \tag{4}$$

where R_{load} is the load resistance and the averaged power density (PD_{ave}) is compared by dividing the averaged power value by the effective area as shown in Figure 3h. Both CS-TENG and the FS-TENG achieve maximum averaged power density values at 10 MΩ; those values are 15.3 and 6.5 mW m^{-2}, respectively.

The normalized power density of the developed FIC-TENG in this study was compared with the recently reported energy harvesters connected to bluff bodies in various fluid flows based on the FIV where the normalized power density is the power density divided by the flow velocity (Figure S9, Supporting Information). In addition, output voltage values according to the flow velocity and dimensions of bluff bodies were compared in Table S1, Supporting Information. The comparison was mainly conducted with piezoelectric energy harvesters because there was no report of a triboelectric energy harvester using the FIV through flow in water and also conducted with wind-driven TENGs using the FIV phenomenon in the air. RMS voltage values of the FIC-TENG are higher than other FIV-based energy harvesters using various bluff bodies in water flow. In addition, the output power of the proposed FIC-TENG can be increased by arranging multiple FIC-TENGs. The recently reported various energy harvesters using bluff bodies in FIV still have lock-in phenomena. Notably, the FIC-TENG developed in this study has a great advantage because the impacting cylinder in the FIC-TENG starts to oscillate at an extremely low flow velocity (0.05 m s^{-1}) and can be applied up to a high flow velocity, which allows the FIC-TENG to be expanded for the wide range of applications such as ocean energy harvesting.

2.3. Demonstration of Collectively Exhaustive Hybrid FIC-TENG

The proposed FIC-TENG has great practical application potential for collectively exhaustive ocean or river energy harvesting through the arrangement of multiple FIC-TENGs to enhance the output power sufficient to supply the required energy consumption of the wireless sensor networks as schematically shown in **Figure 4**a. To demonstrate the collectively exhaustive energy harvesting performance of the FIC-TENG, a water tunnel experiment of the hybrid FIC-TENG was conducted. Figure 4b shows the energy harvesting processes of the hybrid FIC-TENG in a half cycle when the FIC-TENG generates electrical output signals in each TENG mode. The corresponding V signals of the CS-TENGs and the FS-TENG were simultaneously measured with two channels of the oscilloscope (Figure 4c). This demonstrates that continuous energy harvesting is possible with the collectively exhaustive FIC-TENG in the entire time domain in which the cylinder oscillates. Figure 4d shows an optical image of 84 light emitting diodes illuminated by the FIC-TENG. The letters of the FIC-TENG are connected to the CS-TENGs to light up intermittently, and the underline at the bottom is connected to the FS-TENG to light up continuously (Video S2, Supporting Information).

Since the FIC-TENG generates an alternating current (AC) output signal, rectifiers that convert AC signal to direct current (DC) are connected to each TENG, and the charging performances of the CS-TENG, FS-TENG, and hybrid TENG in the FIC-TENG are compared using the same capacitor (Figure 4e). The charging circuit of the capacitor with a capacitance of 100 μF is illustrated in the inset of Figure 4e. The capacitor of 100 μF can be charged to 10 V in only 18 s by utilizing the hybrid mode FIC-TENG. Meanwhile, the same capacitor can be charged to 10 V in 44 and 25 s by using only the FS-TENG and CS-TENG in the FIC-TENG, respectively. That is, the energy harvesting efficiency of the hybrid mode FIC-TENG is greatly improved by using CS-TENG and FS-TENG together, because the time for charging the capacitor is significantly reduced in the same water flow environment. To demonstrate the practical application of the FIC-TENG in the ocean environment, the FIC-TENG was used to convert

© 2021 Wiley-VCH GmbH

16146840, 2022, 3, Downloaded from https://onlinelibrary.wiley.com/doi/10.1002/aenm.202103076 by Korea Advanced Institute Of, Wiley Online Library on [21/11/2022]. See the Terms and Conditions (https://onlinelibrary.wiley.com/terms-and-conditions) on Wiley Online Library for rules of use; OA articles are governed by the applicable Creative Commons License

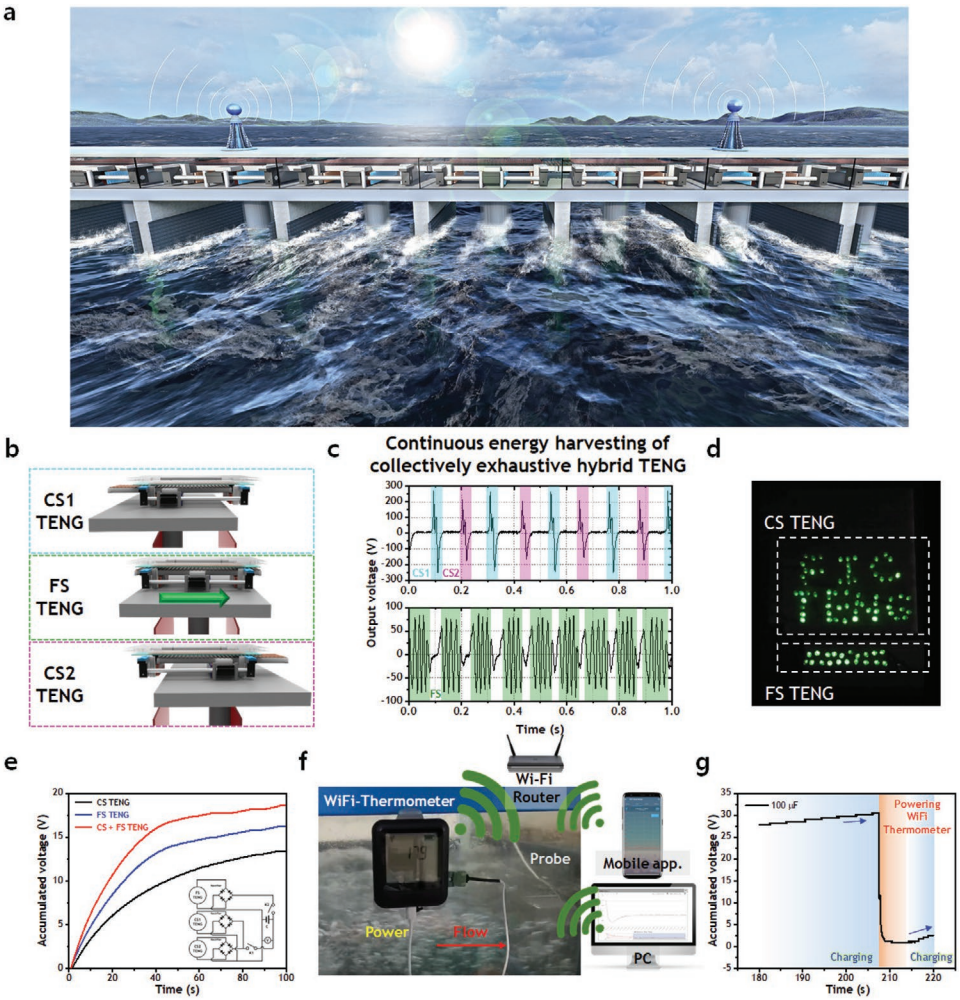


Figure 4. Collectively exhaustive energy harvesting performance and demonstration of FIC-TENG as power source. a) Schematically illustrated practical application of hybrid FIC-TENG for collectively exhaustive ocean energy harvesting through arrangement of multiple FIC-TENGs. b) Schematic diagram of operating processes of collectively exhaustive hybrid FIC-TENG. c) *V* of FS-TENG and CS-TENG at same time. d) Optical image of 84 LEDs powered by FIC-TENG. e) Accumulated voltage profile of 100 μF capacitor with different operating modes of FIC-TENG. f) Optical image and practical application of WiFi thermometer. g) Accumulated voltage profile of 100 μF capacitor for powering WiFi thermometer.

FIV of a cylinder in water flow into electrical energy to power a wireless fidelity (WiFi) thermometer via a power management circuit. The WiFi thermometer has a function of accumulating water temperature data measured every 10 s through its probe and connecting to WiFi to transmit the data once a minute (Figure 4f). The electrical energy generated by the FIC-TENG can be stored in the capacitor through the rectifier, and the stored electrical energy is discharged to power the WiFi thermometer device (Figure 4f and Video S3, Supporting Information). Data transmitted in this way can be viewed on a smartphone application or web via laptop or computer. The accumulated voltage profile of the 100 μF capacitor was measured for powering the WiFi thermometer in Figure 4g. We expect that the FIC-TENG can be applied to supply power to various sensor networks such as temperature, flow velocity, and barometric pressure by arranging multiple FIC-TENGs capable of energy harvesting in an ultrawide flow velocity range of the ocean or river environment.

3. Conclusions

In this work, we report collectively exhaustive hybrid TENGs based on FIV mechanism using a cylinder periodically impacting two side walls in water. The proposed FIC-TENG has a great advantage because the cylinder starts to oscillate at an extremely low flow velocity (0.05 m s^{-1}) and enables continuous oscillation even at a high flow velocity where the isolated cylinder cannot oscillate. The collectively exhaustive hybrid FIC-TENG which utilizes both FS and CS mode TENGs, can effectively convert low frequency mechanical vibrational motion induced by water flow into electrical energy in an ultrawide range of flow velocity due to the change of the flow structure around the impacting cylinder. To enhance the time-averaged power, the FIC-TENG utilizes collision with the side wall, thus the acceleration at the moment of collision is greatly improved, which not only improves the performance of the FS-TENG, but also converts the impact energy into electrical energy with the

© 2021 Wiley-VCH GmbH

16146840, 2022, 3, Downloaded from https://onlinelibrary.wiley.com/doi/10.1002/aenm.202103076 by Korea Advanced Institute Of, Wiley Online Library on [21/11/2022]. See the Terms and Conditions (https://onlinelibrary.wiley.com/terms-and-conditions) on Wiley Online Library for rules of use; OA articles are governed by the applicable Creative Commons License

CS-TENG. As a result, the collectively exhaustive FIC-TENG based on the collision with the side wall demonstrates excellent properties in terms of time-averaged power performance and application suitability in various flow velocity environments. Especially, the FS-TENG has demonstrated a frequency upconversion effect to generate high frequency electrical output resulting from low frequency external mechanical motion, which results in high energy harvesting performance. The structural parameters that affect the energy harvesting performance of the FIC-TENG were systematically investigated and optimized through experiments and FEM electrostatic simulations. At the free-stream velocity of 1.02 m s^{-1}, the peak V_{RMS} values of the FS-TENG and CS-TENG reach 58.6 and 64.1 V, respectively, and the FS-TENG and CS-TENG have maximum averaged power density values of 6.5 and 15.3 mW m^{-2} under a load resistance of 10 MΩ. The proposed collectively exhaustive FIC-TENG system can significantly improve power generation by allowing the arrangement of multiple FIC-TENGs in the ocean, and can be operated on a large scale for applications such as self-powered remote sensor networks.

4. Experimental Section

Fabrication of Freestanding Sliding Mode Triboelectric Nanogenerators: The FS-TENG consisted of a stator with interdigitated electrodes and a slider. The acrylic substrates of the stator and the slider were fabricated by laser cutting machine (C40, Coryart). The interdigitated electrodes were made of 0.025 mm thick copper films (CU000420, Purity: 99.95%, Goodfellow) coated with 0.08 mm thick polytetrafluoroethylene (PTFE) film (ASF-110 FR, Chuckoh); the width and gap of the two electrodes were 3 and 1 mm, respectively. Two electrical wires were connected to each of two electrodes and used for electrical measurements. The slider was designed to alternately contact one electrode of the interdigitated electrodes, and the ladder-shaped substrate was made of acrylic and separated by 4 mm intervals that were 4 mm long (116 mm × 57 mm). Among these materials, copper film, nylon film (AM321017, Goodfellow), and aluminum tape (DTS-02, DUCKSUNG HITECH, thickness 40 μm) were attached only to the spaced portions for comparison. To characterize the FS-TENG, an experiment was performed using a motorized linear stage (X-LSQ150D, Zaber); the total size of the interdigitated electrodes was 57 mm × 47 mm.

Fabrication of Contact-Separation Mode Triboelectric Nanogenerators: The CS-TENG consisted of an electropositive polyurethane-acrylate (PUA) film and an electronegative perfluoropolyether (PFPE) film, each with a 50 nm thick aluminum electrode deposited using electron beam (E-beam) evaporation. The acrylic substrate for electrode attachment was cut into samples with sizes of 3 cm × 3 cm by using a laser cutting machine and electrical wires were connected to each aluminum electrode. The mechanical shaker (S510575, TIRA) was used for applying force to the CS-TENG.

Fabrication of Nano-Patterned Film: To fabricate the nanopatterned surface of the UV curable polymer, PUA, and PFPE, an Si master with line nanopatterns was used. First, resin of UV curable polymer was poured onto the Si master, and a polyethylene terephthalate film was put onto it; the roller was rolled to provide appropriate pressure, and therefore the resin was spread evenly on the Si master and penetrated into the nanopatterns of the Si master. Second, the polymer resin was cured via UV curing process; and, finally, the film was detached from the Si master. Field emission scanning electron microscope (FE-SEM, SU5000, Hitachi) was used to characterize the nanopatterns.

Electrical Measurement: A digital phosphor oscilloscope (DPO 2002B, Tektronix), high voltage probe with an input impedance of 40 MΩ, and a precurrent amplifier (SR570, Stanford Research Systems) were used to measure the output voltage and current.

Finite Element Method Simulation: Finite element method (FEM) with COMSOL multiphysics software was performed to compare the output voltage of the CS mode TENG depending on the nanopattern formation. For comparison, the unit cell size for comparison and the distance between the two contact surfaces were set to 9 μm × 9 μm, and 5 μm, respectively, because the line nanopattern dimensions should be considered.

Flow Visualization: For the water tunnel experiments, the PIV experiments were conducted to compare the wake structure behind the cylinder with and without side walls. A polyamide particle of 50 μm was seeded in the water. To illuminate the particle, a continuous laser (MGL-W-532A, CNI, Co.) was used. The image pairs were taken at 50 frame per second by a high-speed camera (FASTCAM MINI-UX50, Photron Inc.) and cross-correlation was performed by PIVview2C software (version 3.6.0, PIVTEC GmbH). The initial and final window sizes were set to 32 × 32 and 16 × 16 pixels with an overlap of 50%.

Fabrication of Flow-Induced Impacting-Sliding Cylinder Based Triboelectric Nanogenerator: To combine the FS and CS Triboelectric Nanogenerators, an acrylic base plate was fixed on the FIV model. In the FS-TENG, the upper stator (90 mm × 250 mm) and the lower slider (86 mm × 252 mm) were in contact. Interdigitated electrodes with a width of 3 mm and a gap of 1 mm were coated with PTFE film to a thickness of 0.08 mm. Then, the slider was fabricated with a gap of 4 mm and a width of 4 mm. The stator was fixed to the base plate and the slider was attached to the upper side of two bearings and designed to oscillate in the crosswise direction along with the aluminum plate of the FIV system. Two bearings were used to reduce friction between the stator and the slider. Acrylic spacers were placed to control the friction by adjusting the thickness of the spacer between the bearing supports and the acrylic base plate. In the CS-TENG, two acrylic substrates, the fixed and moving parts, were connected to the base plate and the bearing, respectively. The position of the fixed part was adjusted depending on the gap ratio. A nanopatterned PFPE film and PUA film with dimensions of 2 cm × 10 cm with an aluminum electrode were attached to the fixed and moving substrates, respectively.

System Design and Electrical Characterization of Freestanding Sliding Mode Triboelectric Nanogenerator: The FIC-TENG was composed of FS-TENG and CS-TENG. Figure S10, Supporting Information, shows the structure and working mechanism of the FS-TENG. The structure of the FS-TENG features a stator with interdigitated electrodes and a slider (Figure S10a, Supporting Information). Figure S10b, Supporting Information, schematically illustrates the FS-TENG working mechanism which could be explained as a coupling effect of triboelectrification and electrostatic induction. Initially, when the freestanding copper film of the slider was driven to slide in contact with the PTFE film, the PTFE film was negatively charged and the copper film was positively charged due to the difference in electronegativity. Since the area of the copper film was half that of the PTFE film, the charge density of the copper film was twice that of the PTFE film.[25] As the copper film slid and moved on the PTFE film, the number of positive charges of the copper electrode was alternately changed due to electrostatic induction. Therefore, charges flowed between the two interdigitated copper electrodes connected via an external load, producing an AC. The acrylic substrates of the stator and the slider were fabricated using a laser cutting machine. Aluminum, copper, and nylon films were considered as tribopositive materials of the slider; PTFE was considered as the tribonegative material of the stator because it had a helical molecular chain covered by fluorine atoms, a high electron affinity, and a tendency to become highly electronegative in contact with other materials. The short circuit currents (I_{SC}) were compared while each of the films, stators, and sliders had the same dimensions at a sliding speed of 100 mm s^{-1} on the PTFE film (Figure S11, Supporting Information). Therefore, because of its large difference in triboelectric polarity, copper film was finally selected as the tribopositive material of the slider to improve the triboelectrification between two triboelectric surfaces.[26]

Next, a stator with interdigitated electrodes was prepared and fully covered with PTFE film. The slider was designed to alternately contact one electrode of the interdigitated electrodes, which resulted in an increase of current density due to the frequency upconversion effect.[21]

© 2021 Wiley-VCH GmbH

16146840, 2022, 3, Downloaded from https://onlinelibrary.wiley.com/doi/10.1002/aenm.202103076 by Korea Advanced Institute Of, Wiley Online Library on [21/11/2022]. See the Terms and Conditions (https://onlinelibrary.wiley.com/terms-and-conditions) on Wiley Online Library for rules of use; OA articles are governed by the applicable Creative Commons License

The frequency of the AC output signal increased depending on periodic electrode patterns because the AC output signal was generated when the slider moved along the length of the electrode, which improved the energy harvesting performance of the FS-TENG.[13] Electrical characterization of the FS-TENG was conducted by controlling the sliding speed (Figure S12a, Supporting Information). The *V* of the FS-TENG depended on the sliding speed; the faster the slider speed, the more triboelectrification occurred, and the potential difference between the two electrodes increased.[27] Figure S12b, Supporting Information, shows that the *V* of the FS-TENG was enhanced as the sliding speed increased.

The *V* and short circuit current density (J_{SC}) of the FS-TENG were shown at a sliding speed of 500 mm s^{-1} in Figure S13a,b, Supporting Information, respectively. The inset in each figure was a magnified graph corresponding to one cycle of reciprocating motion. Electrical output signals with multiple peaks were generated through a single reciprocating motion, and the overall energy harvesting performance of the FS-TENG improved due to multiple charge separation cycles. The value of J_{SC} of the FS-TENG was calculated by dividing I_{SC} by the contact surface area. The *V* of the FS-TENG had a peak value of 125 V (Figure S13a, Supporting Information), while the J_{SC} peaks at 15.5 mA m^{-2} (Figure S13b, Supporting Information). For electrical characterization of the FS-TENG, the authors measured the peak voltages and peak current densities of the FS-TENG under a series of different resistances (Figure S13c, Supporting Information). The instantaneous power densities (PD_i) of the FS-TENG were calculated using voltages and current densities at different load resistances, showing a maximum peak power density of 0.54 W m^{-2} at a load resistance of 44 MΩ. (Figure S13d, Supporting Information).

Fabrication and Electrical Characterization of Contact and Separation Mode Triboelectric Nanogenerator: To harvest water wave energy effectively, a nanopatterned CS-TENG was fabricated because of its output enhancement effect. In this process, among various nanofabrication methods, nanoimprinting was utilized to fabricate a large-area and defect-free nanopatterned CS-TENG. Interestingly, even though the performance enhancement effects of the nanopatterns on the CS-TENG device were studied in the previous literature[28] and there were many nanopatterning methods, nanoimprinting had not been actively applied to TENG devices because of its fabrication difficulty. The conventional top–down nanofabrication processes such as E-beam lithography and focused ion beam milling required extremely expensive equipment and had low throughput. In addition, most bottom–up nanopatterning methods (e.g., block copolymer lithography) were not suitable for large-area patterning because they produce many defects. To overcome these limitations, a nanoimprinting process was rationally selected for fabricating the nanopatterned CS-TENG in this study because this material could be effectively produced by low-cost, large-area, and defect-free nanopatterning.

The CS-TENG consisted of an electropositive PUA film and an electronegative PFPE film as counter materials, each with a 50 nm thick aluminum electrode deposited by E-beam evaporation (Figure S14a, Supporting Information). The acrylic substrate for the CS-TENG was cut using a laser cutting machine. To enhance the triboelectric charge density, the line nanopatterns were introduced in PUA and PFPE.[29] Figure S14b, Supporting Information, schematically depicts the detailed fabrication steps of the nanopatterned thin film and E-beam evaporation process for electrode deposition. A FE-SEM was used to characterize the nanopatterns in the inset of Figure S14a, Supporting Information.

Figure S14c, Supporting Information, depicts the working mechanism of the CS-TENG. When the PUA and the PFPE were in contact, the PUA was positively charged and the PFPE was negatively charged due to triboelectrification. As the contact surfaces separate, an electrical output signal was generated between the two electrodes to maintain electrostatic equilibrium. In the case of approaching for contact again, the opposite current flowed between the two electrodes, indicating that an AC signal was generated through the reciprocating CS motion. Figure S14d, Supporting Information, shows a fabricated sample of nanopatterned CS-TENG that had a rainbow diffraction pattern. Electrostatic simulation through FEM was conducted to demonstrate the performance improvement of the CS-TENG due to the introduction of nanopatterns (Figure S15, Supporting Information). In addition, CS-TENGs with different dimensions of line-nanopatterned films were experimentally investigated to optimize the energy harvesting performance while varying the length and space of the line nanopattern. Samples with different lengths and spaces were named according to length and space. For example, a line-nanopatterned film having a length of 200 nm and a space of 200 nm was specified as 200/200; the surfaces of the fabricated nanopatterned films were characterized through FE-SEM (Figure S16, Supporting Information). PFPE film had an excellent electronegativity because it contained fluorine, and was similar to PTFE film in its structure.[30] To confirm the effect contributing to triboelectrification performance, the *V* comparison was performed with the same PUA film between a flat PFPE film and a flat PTFE film, and very similar results were obtained (Figure S17a, Supporting Information). Therefore, PFPE was selected as tribonegative material in the CS-TENG because it was a UV curable polymer that could be nanopatterned and also had excellent performance due to a high electronegativity.

From a comparison of *V* according to the different lengths and spaces of the line nanopatterns, the highest *V* was obtained in the case of 200/200, which had both the smallest length and space (Figure S17b,c, Supporting Information). The improvement of *V* could be attributed to the increase of the effective contact area as both the length and space decrease. Furthermore, experimental results were in good agreement with the analytical results obtained through FEM electrostatic simulation with different dimensions of line nanopatterns (Figure S17d, Supporting Information). Figure S17e,f, Supporting Information, shows the *V* when changing the contact force and frequency, respectively. Experiments for electrical characterization of the CS-TENG were conducted with a contact force of 8 N and a frequency of 5 Hz.

Notably, the *V* of the CS-TENG using line-nanopatterned PUA and PFPE films improved more than three times compared with that of CS-TENG using flat PUA and PFPE films (Figure S18a, Supporting Information). The significant improvement of the *V* of the nanopatterned CS-TENG could be attributed to the introduction of the line nanopattern with large effective contact area and surface roughness at nanoscale.[31] The *V* and J_{SC} values of the CS-TENG were measured and the inset of each figure was a magnified graph of one cycle during the repeated CS motion (Figure S18b,c, Supporting Information). The peak value of the *V* of the CS-TENG was about 600 V, and the peak value of the J_{SC} of the CS-TENG was about 3 mA m^{-2}. For the electrical characterization of the CS-TENG, the current and voltage were measured under various load resistances, with results shown in Figure S18d, Supporting Information. The PD_i was calculated according to the load resistance, and the fabricated CS-TENG was found to have the maximum peak power density of 0.12 W m^{-2} at 3.4 MΩ (Figure S18e, Supporting Information). Figure S18f, Supporting Information, shows a stable *V* of the CS-TENG even in a long-term experiment of 5000 cycles, which confirmed the reliable stability of the CS-TENG without degradation during long-term operation; this good performance was possible because there was no surface damage due to local stress concentration on the contact surface. Rather, through repeated operation, the *V* increased slowly compared with the initial state, because the surface charge of the film was saturated up to the maximum charge owing to continuous triboelectrification.

Supporting Information

Supporting Information is available from the Wiley Online Library or from the author.

Acknowledgements

J.-S.K. and J.K. contributed equally to this work. This work was supported by Creative Research Initiative Program (2015R1A3A2028975) and funded by National Research Foundation of Korea (NRF). This work was

© 2021 Wiley-VCH GmbH

16146840, 2022, 3, Downloaded from https://onlinelibrary.wiley.com/doi/10.1002/aenm.202103076 by Korea Advanced Institute Of, Wiley Online Library on [21/11/2022]. See the Terms and Conditions (https://onlinelibrary.wiley.com/terms-and-conditions) on Wiley Online Library for rules of use; OA articles are governed by the applicable Creative Commons License

supported by the Defense Acquisition Program Administration and the Agency for Defense Development (ADD) in Korea under the contract UD200011DD. This research was supported by the Human Resources Program in Energy Technology of the Korea Institute of Energy Technology Evaluation and Planning (KETEP) granted financial resource from the Ministry of Trade, Industry and Energy, Republic of Korea (No. 20204030200050).

Conflict of Interest

The authors declare no conflict of interest.

Data Availability Statement

The data that support the findings of this study are available from the corresponding author upon reasonable request.

Keywords

flow-induced oscillation, hybrid modes, impact and sliding, ocean energy harvesters, triboelectric nanogenerators

Received: October 3, 2021
Revised: November 3, 2021
Published online: December 4, 2021

[1] a) S. Guo, Q. Liu, J. Sun, H. Jin, *Renewable Sustainable Energy Rev.* **2018**, *91*, 1121; b) K. Hansen, C. Breyer, H. Lund, *Energy* **2019**, *175*, 471; c) S. Sen, S. Ganguly, *Renewable Sustainable Energy Rev.* **2017**, *69*, 1170.

[2] a) Y. Chen, Y. Cheng, Y. Jie, X. Cao, N. Wang, Z. L. Wang, *Energy Environ. Sci.* **2019**, *12*, 2678; b) Y. Zhang, J. Cao, H. Zhu, Y. Lei, *Energy Convers. Manage.* **2019**, *180*, 811; c) K. Fan, M. Cai, F. Wang, L. Tang, J. Liang, Y. Wu, H. Qu, Q. Tan, *Energy Convers. Manage.* **2019**, *198*, 111820.

[3] a) W. Liu, Z. Wang, G. Wang, G. Liu, J. Chen, X. Pu, Y. Xi, X. Wang, H. Guo, C. Hu, Z. L. Wang, *Nat. Commun.* **2019**, *10*, 1426; b) C. Wu, A. C. Wang, W. Ding, H. Guo, Z. L. Wang, *Adv. Energy Mater.* **2019**, *9*, 1802906; c) H.-J. Yoon, M. Kang, W. Seung, S. S. Kwak, J. Kim, H. T. Kim, S.-W. Kim, *Adv. Energy Mater.* **2020**, *10*, 2000730; d) J. Kim, H. Cho, M. Han, Y. Jung, S. S. Kwak, H.-J. Yoon, B. Park, H. Kim, H. Kim, J. Park, S.-W. Kim, *Adv. Energy Mater.* **2020**, *10*, 2002312; e) X. Liu, K. Zhao, Y. Yang, *Nano Energy* **2018**, *53*, 622; f) X. Zhao, B. Chen, G. Wei, J. M. Wu, W. Han, Y. Yang, *Adv. Mater. Technol.* **2019**, *4*, 1800723; g) B. Chen, Y. Yang, Z. L. Wang, *Adv. Energy Mater.* **2018**, *8*, 1702649.

[4] a) J. Zhang, Z. Fang, C. Shu, J. Zhang, Q. Zhang, C. Li, *Sens. Actuators, A* **2017**, *262*, 123; b) F. Qian, T.-B. Xu, L. Zuo, *Energy* **2019**, *189*, 116140; c) D. W. Wang, J. L. Mo, X. F. Wang, H. Ouyang, Z. R. Zhou, *Energy Convers. Manage.* **2018**, *171*, 1134.

[5] a) M. P. Lumb, S. Mack, K. J. Schmieder, M. González, M. F. Bennett, D. Scheiman, M. Meitl, B. Fisher, S. Burroughs, K.-T. Lee, J. A. Rogers, R. J. Walters, *Adv. Energy Mater.* **2017**, *7*, 1700345; b) Y. Liu, N. Sun, J. Liu, Z. Wen, X. Sun, S.-T. Lee, B. Sun, *ACS Nano* **2018**, *12*, 2893; c) D. Yoo, S.-C. Park, S. Lee, J.-Y. Sim, I. Song, D. Choi, H. Lim, D. S. Kim, *Nano Energy* **2019**, *57*, 424.

[6] a) K. Zhang, Y. Wang, Y. Yang, *Adv. Funct. Mater.* **2019**, *29*, 1806435; b) Y. Ji, K. Zhang, Z. L. Wang, Y. Yang, *Energy Environ. Sci.* **2019**, *12*, 1231.

[7] a) A. Khaligh, O. Onar, *Energy Harvesting: Solar, Wind, and Ocean Energy Conversion Systems*, CRC Press, Boca Raton, FL **2017**; b) L. Xu, T. Jiang, P. Lin, J. J. Shao, C. He, W. Zhong, X. Y. Chen, Z. L. Wang, *ACS Nano* **2018**, *12*, 1849.

[8] a) M. Xu, T. Zhao, C. Wang, S. L. Zhang, Z. Li, X. Pan, Z. L. Wang, *ACS Nano* **2019**, *13*, 1932; b) D. Y. Kim, H. S. Kim, D. S. Kong, M. Choi, H. B. Kim, J.-H. Lee, G. Murillo, M. Lee, S. S. Kim, J. H. Jung, *Nano Energy* **2018**, *45*, 247; c) Y. Zi, H. Guo, Z. Wen, M.-H. Yeh, C. Hu, Z. L. Wang, *ACS Nano* **2016**, *10*, 4797.

[9] a) W. Liu, L. Xu, T. Bu, H. Yang, G. Liu, W. Li, Y. Pang, C. Hu, C. Zhang, T. Cheng, *Nano Energy* **2019**, *58*, 499; b) G. Liu, H. Guo, S. Xu, C. Hu, Z. L. Wang, *Adv. Energy Mater.* **2019**, *9*, 1900801; c) F. Xi, Y. Pang, G. Liu, S. Wang, W. Li, C. Zhang, Z. L. Wang, *Nano Energy* **2019**, *61*, 1; d) P. Chen, J. An, S. Shu, R. Cheng, J. Nie, T. Jiang, Z. L. Wang, *Adv. Energy Mater.* **2021**, *11*, 2003066; e) L. Gao, X. Chen, S. Lu, H. Zhou, W. Xie, J. Chen, M. Qi, H. Yu, X. Mu, Z. L. Wang, Y. Yang, *Adv. Energy Mater.* **2019**, *9*, 1902725.

[10] a) G. Zhu, C. Pan, W. Guo, C.-Y. Chen, Y. Zhou, R. Yu, Z. L. Wang, *Nano Lett.* **2012**, *12*, 4960; b) G. Zhu, Z.-H. Lin, Q. Jing, P. Bai, C. Pan, Y. Yang, Y. Zhou, Z. L. Wang, *Nano Lett.* **2013**, *13*, 847.

[11] F.-R. Fan, Z.-Q. Tian, Z. L. Wang, *Nano Energy* **2012**, *1*, 328.

[12] S. Wang, L. Lin, Y. Xie, Q. Jing, S. Niu, Z. L. Wang, *Nano Lett.* **2013**, *13*, 2226.

[13] Y. Xie, S. Wang, S. Niu, L. Lin, Q. Jing, J. Yang, Z. Wu, Z. L. Wang, *Adv. Mater.* **2014**, *26*, 6599.

[14] S. Niu, Y. Liu, S. Wang, L. Lin, Y. S. Zhou, Y. Hu, Z. L. Wang, *Adv. Funct. Mater.* **2014**, *24*, 3332.

[15] a) C.-D. Le, C.-P. Vo, T.-H. Nguyen, D.-L. Vu, K. K. Ahn, *Nano Energy* **2021**, *80*, 105571; b) B. Wang, Y. Wu, Y. Liu, Y. Zheng, Y. Liu, C. Xu, X. Kong, Y. Feng, X. Zhang, D. Wang, *ACS Appl. Mater. Interfaces* **2020**, *12*, 31351.

[16] a) H. Wang, Q. Zhu, Z. Ding, Z. Li, H. Zheng, J. Fu, C. Diao, X. Zhang, J. Tian, Y. Zi, *Nano Energy* **2019**, *57*, 616; b) A. Chandrasekhar, V. Vivekananthan, S.-J. Kim, *Nano Energy* **2020**, *69*, 104439; c) J. An, Z. M. Wang, T. Jiang, X. Liang, Z. L. Wang, *Adv. Funct. Mater.* **2019**, *29*, 1904867; d) Y. Pang, S. Chen, Y. Chu, Z. L. Wang, C. Cao, *Nano Energy* **2019**, *66*, 104131; e) K. Xia, J. Fu, Z. Xu, *Adv. Energy Mater.* **2020**, *10*, 2000426.

[17] B. Zanuttigh, E. Angelelli, A. Kortenhaus, K. Koca, Y. Krontira, P. Koundouri, *Renewable Energy* **2016**, *85*, 1271.

[18] a) J. H. Lee, M. M. Bernitsas, *Ocean Eng.* **2011**, *38*, 1697; b) E. S. Kim, M. M. Bernitsas, R. A. Kumar, *J. Offshore Mech. Arct. Eng.* **2013**, *135*, 021802; c) A. Mehmood, A. Abdelkefi, M. R. Hajj, A. H. Nayfeh, I. Akhtar, A. O. Nuhait, *J. Sound Vib.* **2013**, *332*, 4656.

[19] a) T. Sarpkaya, *J. Fluids Struct.* **2004**, *19*, 389; b) C. H. K. Williamson, R. Govardhan, *Annu. Rev. Fluid Mech.* **2004**, *36*, 413.

[20] a) H. D. Akaydin, N. Elvin, Y. Andreopoulos, *Smart Mater. Struct.* **2012**, *21*, 025007; b) X. Gao, W. Shih, W. Y. Shih, *IEEE Trans. Ind. Electron.* **2013**, *60*, 1116; c) H. L. Dai, A. Abdelkefi, L. Wang, *Nonlinear Dyn.* **2014**, *77*, 967.

[21] K.-W. Han, J.-N. Kim, A. Rajabi-Abhari, V.-T. Bui, J.-S. Kim, D. Choi, I.-K. Oh, *Adv. Energy Mater.* **2021**, *11*, 2002929.

[22] Z.-J. Zhao, J. Ahn, J. Ko, Y. Jeong, M. Bok, S. H. Hwang, H.-J. Kang, S. Jeon, J. Choi, I. Park, J.-H. Jeong, *ACS Appl. Mater. Interfaces* **2021**, *13*, 3358.

[23] H. Zhang, C. Zhang, J. Zhang, L. Quan, H. Huang, J. Jiang, S. Dong, J. Luo, *Nano Energy* **2019**, *61*, 442.

[24] Z. Wang, W. Liu, J. Hu, W. He, H. Yang, C. Ling, Y. Xi, X. Wang, A. Liu, C. Hu, *Nano Energy* **2020**, *69*, 104452.

[25] S. Wang, Y. Xie, S. Niu, L. Lin, Z. L. Wang, *Adv. Mater.* **2014**, *26*, 2818.

[26] D. Liu, X. Yin, H. Guo, L. Zhou, X. Li, C. Zhang, J. Wang, Z. L. Wang, *Sci. Adv.* **2019**, *5*, eaav6437.

© 2021 Wiley-VCH GmbH

16146840, 2022, 3, Downloaded from https://onlinelibrary.wiley.com/doi/10.1002/aenm.202103076 by Korea Advanced Institute Of, Wiley Online Library on [21/11/2022]. See the Terms and Conditions (https://onlinelibrary.wiley.com/terms-and-conditions) on Wiley Online Library for rules of use; OA articles are governed by the applicable Creative Commons License

[27] A. N. Ravichandran, F. Depoutot, E. Kharbouche, M. Hamand, M. Ramuz, S. Blayac, *Nano Energy* **2021**, *83*, 105796.
[28] J. Ahn, Z.-J. Zhao, J. Choi, Y. Jeong, S. Hwang, J. Ko, J. Gu, S. Jeon, J. Park, M. Kang, D. V. Del Orbe, I. Cho, H. Kang, M. Bok, J.-H. Jeong, I. Park, *Nano Energy* **2021**, *85*, 105978.
[29] Z.-J. Zhao, J. Ahn, S. H. Hwang, J. Ko, Y. Jeong, M. Bok, H.-J. Kang, J. Choi, S. Jeon, I. Park, J.-H. Jeong, *ACS Nano* **2021**, *15*, 503.
[30] Y. H. Kwon, S.-H. Shin, J.-Y. Jung, J. Nah, *Nanotechnology* **2016**, *27*, 205401.
[31] H. S. Wang, C. K. Jeong, M.-H. Seo, D. J. Joe, J. H. Han, J.-B. Yoon, K. J. Lee, *Nano Energy* **2017**, *35*, 415.

© 2021 Wiley-VCH GmbH

16146840, 2022, 3, Downloaded from https://onlinelibrary.wiley.com/doi/10.1002/aenm.202103076 by Korea Advanced Institute Of, Wiley Online Library on [21/11/2022]. See the Terms and Conditions (https://onlinelibrary.wiley.com/terms-and-conditions) on Wiley Online Library for rules of use; OA articles are governed by the applicable Creative Commons License